Ultramicroscopy 165 (2016) 42–50

Contents lists available at ScienceDirect

Ultramicroscopy

journal homepage: www.elsevier.com/locate/ultramic

Pixelated detectors and improved efficiency for magnetic imaging in STEM differential phase contrast

Matus Krajnak, Damien McGrouther, Dzmitry Maneuski, Val O' Shea, Stephen McVitie *

Scottish Universities Physics Alliance, School of Physics and Astronomy, University of Glasgow, Glasgow G12 8QQ, United Kingdom

ARTICLE INFO

Article history:
Received 21 August 2015
Received in revised form
8 March 2016
Accepted 22 March 2016
Available online 7 April 2016

Keywords:
Differential phase contrast
STEM
Magnetic thin films
4D electron microscopy

ABSTRACT

The application of differential phase contrast imaging to the study of polycrystalline magnetic thin films and nanostructures has been hampered by the strong diffraction contrast resulting from the granular structure of the materials. In this paper we demonstrate how a pixelated detector has been used to detect the bright field disk in aberration corrected scanning transmission electron microscopy (STEM) and subsequent processing of the acquired data allows efficient enhancement of the magnetic contrast in the resulting images. Initial results from a charged coupled device (CCD) camera demonstrate the highly efficient nature of this improvement over previous methods. Further hardware development with the use of a direct radiation detector, the Medipix3, also shows the possibilities where the reduction in collection time is more than an order of magnitude compared to the CCD. We show that this allows subpixel measurement of the beam deflection due to the magnetic induction. While the detection and processing is data intensive we have demonstrated highly efficient DPC imaging whereby pixel by pixel interpretation of the induction variation is realised with great potential for nanomagnetic imaging.

1. Introduction

Differential phase contrast (DPC) is an imaging technique which enables direct imaging of electromagnetic fields in the scanning transmission electron microscope (STEM). It has been applied very effectively across a wide length range and has facilitated atomic scale electric fields [1] and magnetic domain and magnetic stray field observations [2]. Electric field imaging is generally performed in standard high resolution mode while magnetic imaging almost always requires a low magnetic field environment at the sample. For the latter, the objective lens of the microscope is either switched off or only weakly excited. Detection and the resultant imaging of electromagnetic fields in DPC is most easily understood in terms of the classical sample induced Lorentz force deflection of the incident electron beam. However, understanding of the fundamental basis for DPC imaging requires proper consideration of the phase-shift caused by the electromagnetic fields to the wavefunction of transmitted electrons. Fields due to scalar electrostatic potentials, e.g. atomic electronic potentials, dielectric moments and extrinsic applied electric fields, induce phase changes through Coulomb interaction with the beam. Magnetic interaction with the electron beam, arising from magnetisation due to atomic magnetic moments, and intrinsic stray or extrinsic applied magnetic fields, is understood through the quantum mechanical Aharonov–Bohm effect [3]. Thus, proper calculation or simulation of DPC images must be based on a wave-optical approach.

Detection of the electron beam deflection/phase effect has traditionally been achieved with a segmented detector [4,5] from which differential phase contrast is obtained by forming difference signals from opposing segments [6]. The geometries employed include bi-split [4], quadrant [7] and annular quadrant [8] with significant performance improvements being gained for imaging of polycrystalline magnetic thin film structures with the latter. In such films contrast arising at grain boundaries can produce contrast variations as strong, or stronger, than those arising from the intrinsic magnetisation and contributes unwanted signal variation in the differential phase image.

In this paper we demonstrate that the highest magnetic DPC imaging performance is obtained when a pixelated detector is used to collect the entire bright field disc of electrons transmitted by the sample. Specifically, we show that for magnetic nanostructures fabricated from polycrystalline thin films almost complete separation of crystal structure contrast from the magnetic phase contrast can be achieved. In the following sections we discuss the theoretical basis for DPC contrast in magnetic samples, the effect of segmented detector geometry on the contrast transfer function before going on to show results from processing of DPC datasets obtained using pixelated detectors. The results demonstrate the potential for pixelated detectors for samples with strong

* Corresponding author.
E-mail address: stephen.mcvitie@glasgow.ac.uk (S. McVitie).

http://dx.doi.org/10.1016/j.ultramic.2016.03.006

polycrystalline diffraction contrast and we discuss the image processing methods which allow the magnetic signal to be extracted from the datasets.

2. Theory

Differential phase contrast of magnetic materials can be interpreted in simple terms on a classical level due to applied forces. However a quantum mechanical wave-optical approach may also be considered, which although less intuitive allows image calculation from simulations by simple Fourier methods. Firstly we reproduce the arguments to show these approaches to be equivalent and then discuss how we can use this information to propose methods to extract more efficiently the magnetic information present when using a pixelated detector system. In the simple classical approach we consider what happens when an electron beam passes through a uniformly magnetised film of thickness t with a saturation induction of B_S, like that shown in Fig. 1(a). As the film is magnetised in-plane the Lorentz force $\mathbf{F} = q(\mathbf{v} \times \mathbf{B})$ leads to a magnetic deflection angle β_L given by:

$$\beta_L = -\frac{e\lambda}{h} B_S t, \tag{1}$$

where e is the magnitude of electronic charge, λ is the electron wavelength and h is the Plancks constant [6]. Typically for a 10 nm thick film of permalloy (saturation induction 1.0 T) and using 200 kV electrons this gives a value of 6.4 μrad. This value is around three orders of magnitude less than a typical Bragg scattering angle. In general the induction may not be uniform and would then involve an integral along the electron path (**dl**). In vector form this is given by:

$$\beta_L = -\frac{e\lambda}{h} \int \mathbf{B} \times \mathbf{dl}. \tag{2}$$

Eqs. (1) and (2) provide an intuitive interpretation of the Lorentz effect in that detection of the magnitude and direction of the deflection of the beam allows the integrated induction, perpendicular to the beam, to be measured. Alternatively we may consider the effect of the phase of the electron beam by the magnetic potential in and around the sample. For a magnetic material this is given by the Aharonov–Bohm effect [3] which relates the phase change, $\Delta\phi$, between 2 electrons following paths as shown in Fig. 1 (b):

$$\Delta\phi = -2\pi\frac{e}{h}\int \mathbf{A}\cdot\mathbf{dl} = -2\pi\frac{e}{h}\int \mathbf{B}\cdot\mathbf{dS}. \tag{3}$$

The line integral of the vector equation is not so intuitive as it involves the not so commonly used magnetic vector potential **A**. However using vector calculus this can be converted into a surface integral (over **dS**) of the magnetic flux (and hence the more intuitive quantity **B**) through the surface connecting the electron paths. If we then consider the uniformly magnetised thin film as shown in Fig. 1(b) the linear phase variation in the x direction can then be written as:

$$\phi = -2\pi\frac{e}{h} B_S t x. \tag{4}$$

In wave optical theory this phase appears in the wave function of the beam just after it has traversed the sample as a complex exponential ($\exp(i\phi)$). The phase variation, for such a uniformly magnetised thin film considered here, is linear in x, i.e. $\phi = 2\pi\, k_L\, x$ with the spatial frequency k_L associated with the integrated magnetic induction. In STEM the probe forming aperture defines the probe semi-angle α of the focused probe. In the absence of a sample the probe projects a uniform disk on to the detector plane with a radius in reciprocal space of $k_\alpha = (\alpha/\lambda)$. This is shown in Fig. 1(c) when a CCD camera is used to image the bright field electron disc (further details in next section). The detector plane can be considered in angular terms or equivalently in spatial frequency. The equivalence of the classical and quantum approaches can be shown by taking the derivative of Eq. (4) with respect to x which results in (for the 1D case for a uniformly magnetised film):

$$\frac{\partial\phi}{\partial x} = -2\pi\frac{e}{h} B_S t = -\frac{2\pi}{\lambda}\beta_L = -2\pi k_L. \tag{5}$$

In terms of STEM imaging the presence of a magnetically induced phase gradient is detected through the bright field disc, with form $S(k)$ in the detector plane being displaced to $S(k - k_L)$. It should be noted that magnetic thin films are generally regarded as strong phase objects. As an example the deflection angle calculated earlier for a uniformly magnetised 10 nm Permalloy film imaged with 200 kV electrons corresponds to a phase gradient of 2π every 350 nm in the direction transverse to the magnetisation. However the spatial frequency, $(350\ \text{nm})^{-1}$, associated with the phase gradients due to magnetic film is very low and often only a small fraction of the maximum spatial frequency associated with the probe, typically $(1\text{–}5\ \text{nm})^{-1}$. We discuss this further now in

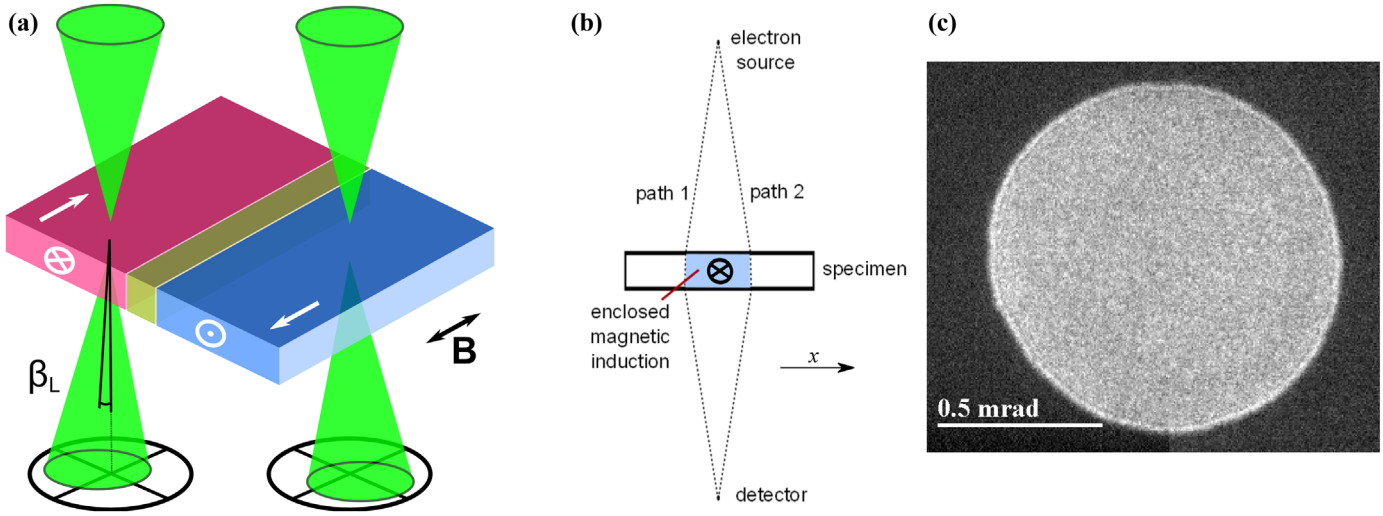

Fig. 1. (a) STEM schematic of electron beam passing through regions of a uniformly magnetised thin film. (b) Beam path of two electrons considered for electron phase showing enclosed magnetic flux in the specimen between the 2 trajectories. (c) Image of central diffraction disk in STEM mode captured on CCD camera.

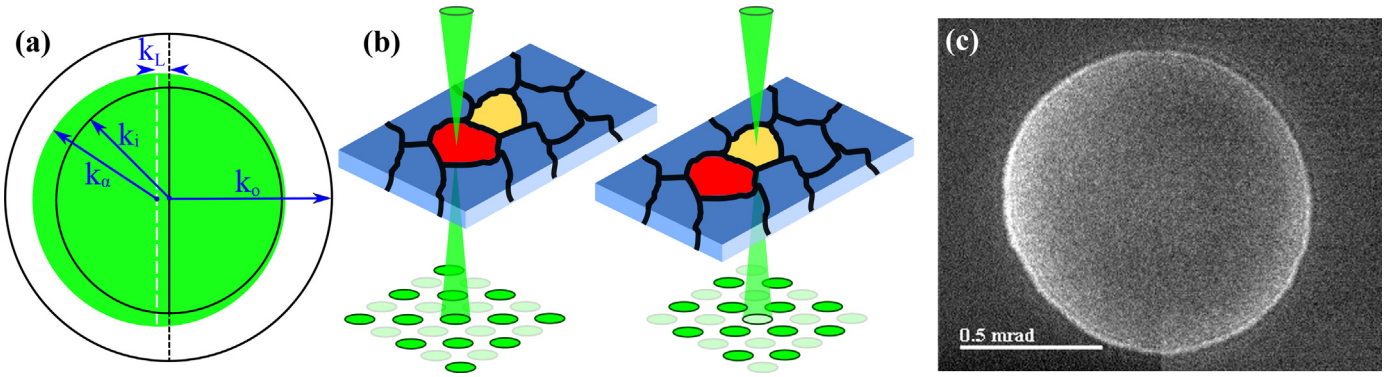

Fig. 2. (a) Schematic of split annular detector showing important spatial frequencies; from magnetic film (k_L), probe (k_α) and inner and outer annular detector radius (k_i and k_o respectively), (b) Bragg condition change between differently oriented grains, and (c) example of central diffraction disk imaged with CCD camera at grain boundary.

terms of detector geometry and contrast transfer functions.

For a basic understanding of the basis of magnetic DPC imaging we consider a split annular detector where the bright field disk has been displaced due to presence of a magnetic thin film as shown in Fig. 2(a). The important parameters here are the spatial extent of the probe k_α, the size of the inner radius of the annulus k_i, outer annulus k_o and the displacement of the disk due to magnetic film k_L. In this case we see that the disk displacement is very small, as argued earlier, and also the hole is still covered by the disk. A simple understanding here is that by taking the difference of the intensity falling on the left half minus the right half we get a signal which is proportional to the phase gradient. Due to the small displacement of the disk we can make the approximation that the left hand signal is proportional to $(\pi k_\alpha^2)/2 + 2k_\alpha k_L - (\pi k_i^2)/2$. The right hand signal is given by $(\pi k_\alpha^2)/2 - 2k_\alpha k_L - (\pi k_i^2)/2$. The difference signal is therefore $4k_\alpha k_L$, which is linearly proportional to the magnetic spatial frequency or deflection angle. Interestingly the presence of the hole does not affect the magnitude of the difference signal. The effect of the hole was discussed in detail for magnetic imaging [8] when consideration of the high spatial frequency contrast resulting from small (5–10 nm) crystallites was shown to be reduced with the annular detector arrangement. In that paper the contrast transfer function was calculated based on a representation of perfect sinusoidal phase variations resulting in the concept of overlapping disks which is a commonly used principle for calculations of contrast transfer functions [4,9–11]. The result was the proposal of modified DPC imaging whereby the size of the bright field disk relative to the hole (k_i/k_α) was optimised to enhance the low spatial frequency magnetic signal to the high spatial frequency contribution from the crystallites. This can be illustrated simply as shown in Fig. 2(b) where the effect of grain orientation is highlighted schematically. Differently oriented grains result in different Bragg scattering conditions, while if both are magnetised in the same direction they will also deflect the beam by the same amount. Of course the magnetic deflection (μrads) is tiny compared to the Bragg scattering angles (mrads) If it was only the case of a different intensity in the bright field disk for each grain the difference signal could be normalised with the total signal falling on the quadrant detector. However it is apparent that intensity variations within the disk are present as seen in Fig. 2(c), when the disk overlaps more than one grain. The effect of the hole in an annular detector will reduce this contribution but for many very thin polycrystalline magnetic films even this modified DPC is insufficient to bring out the magnetic contrast strongly. Therefore the effects seen at grain boundaries or multiple scattering events are a real source of difficulties in interpreting small beam displacement. With aberration correction [12,13] enabling a spatial resolution of 1 nm (with the objective lens off or weakly excited) for imaging of magnetic structure [14,15] this problem has become a significant and limiting one.

In the next section we describe how these effects can be overcome by the use of pixelated detection. In order to do this we assume that the disk movement is due only to magnetic phase effects and that intensity variations within the disk arise from differential scattering from grains. These assumptions are justified by the results obtained and further comment is given in the conclusions section.

3. Experimental details

All the imaging described in this paper was carried out on a JEOL Atomic Resolution Microscope (JEM-ARM200F), operating at 200 kV [15]. This microscope is equipped with a cold field emission gun and a CEOS (Corrected Electron Optical Systems GmbH) probe corrector for STEM imaging. DPC imaging was carried out with the HR objective lens polepiece switched off with the sample then sitting in the remanent field of the lens which is around 150 Oe out of plane. An 8 segment silicon photodiode array detector (supplied by Deben UK Ltd. comprising a solid quadrant inside a contiguous annular quadrant) was used for the DPC imaging. The signal from the detectors was converted and amplified using the “Superfast” amplifier (Andrew Armit Designs). The 8 detected signals were acquired, mixed and displayed via four Gatan Digiscan II units which mean that up to 16 signal combinations may be displayed simultaneously. An example of the images obtained from this system is shown in Fig. 3 which shows images taken at two different magnifications of a square of 30 nm thick permalloy with side length of 1 μm fabricated by FIB lithography. Different signals from opposite segments of the detector are used to map orthogonal components of integrated induction, the mapping directions indicated by the double headed arrows. Permalloy is a soft magnetic material with the domain structure determined by a balance between the ferromagnetic exchange energy and the magnetostatic energy. In this case a flux closure domain structure is observed in the Permalloy with the magnetisation following the edges to reduce magnetostatic energy. This results in 4 well-defined domains with a rotation vortex domain structure in the centre. This is very apparent in the lower magnification images in Figs. 3(a) and (b). However when the centre of the square is imaged at higher magnification very strong diffraction effects are seen from the polycrystalline grain structure of the material, shown in Figs. 3(c) and (d). The underlying magnetic contrast is just about visible, however the intensity variation on the 5–10 nm scale virtually swamps the magnetic contrast. This small scale variation is due to the differential Bragg scattering from the face centred cubic, randomly oriented grains illustrated schematically in Fig. 2.

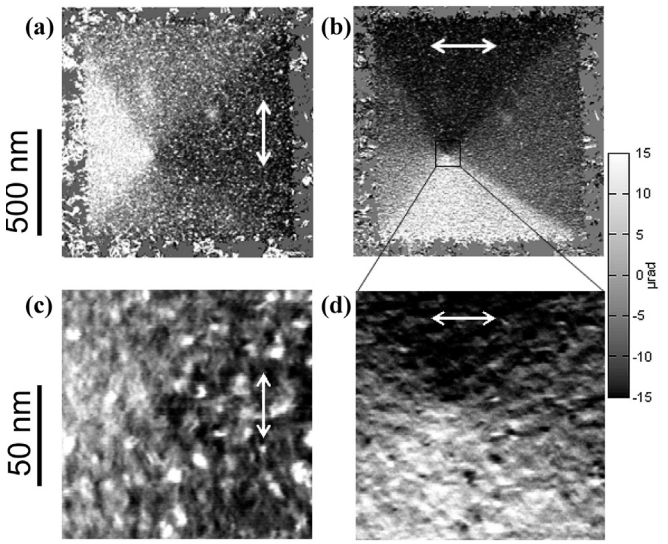

Fig. 3. Example of segmented DPC detection, 30 nm thick 1 μm sized square permalloy structure, (a) and (b) 2 orthogonal components of integrated magnetic induction; (c) and (d) detail of the same region showing diffraction effects visible at higher magnification.

Detection of the central diffraction disk by a pixelated detector was initially performed on a CCD camera (Gatan Orius). In itself the CCD camera is not an ideal imaging system for STEM e.g. due to charge spreading and its low frame rate. However it can be used to demonstrate the principle and advantages of pixelated detection in DPC. The Orius camera has 11MPix resolution (4008×2672 pixels), which was binned $4\times$ to reduce the large amount of data needed for a diffraction pattern acquired for each scan point in STEM and charge spreading. The maximum frame rate of the camera (14 fps) is also a limiting factor and as such we chose a beam dwell time of 50 ms resulting in an acquisition time of 12 min for a 100×100 pixel image, taking account of the readout time of the camera. Such long acquisition times are not practical with stability and sample drift issues if a larger image set were to be taken. To achieve greater than an order of magnitude reduction in pixel dwell time, and therefore a corresponding increase in scan-rate, we have installed a small, 256×256 pixel direct solid state detector. The Medipix3 detector [16] is a counting detector originally designed for X-ray photon imaging. It has a unique architecture that combines, for each pixel, analogue and digital circuitry that can be optimised for the detection of single 200 keV electrons. In principle a maximum frame rate of 3000 fps is possible. However, the actual frame-rate depends on the performance of the readout system that is connected to the detector. In our installation, using the MERLIN readout system [17] frame rates of up 1200 fps are possible for short bursts. Sustained readouts of 500 fps were employed for pixelated STEM detection.

All imaging experiments were conducted on a 20 nm thick permalloy (NiFe) film doped with 5% platinum, which was deposited on Si_3N_4 support membrane.

4. Data analysis

Conventional DPC imaging was performed using a beam convergence semi-angle $\alpha = 0.537$ mrad with corresponding spatial frequency $(5\ \text{nm})^{-1}$.

Employing a camera length of 300 cm the central diffraction disk impinged only on the inner 4 quadrants of the 8 quadrant detector, as shown schematically in Fig. 4(a). Components of the beam deflection and hence the integrated induction were mapped

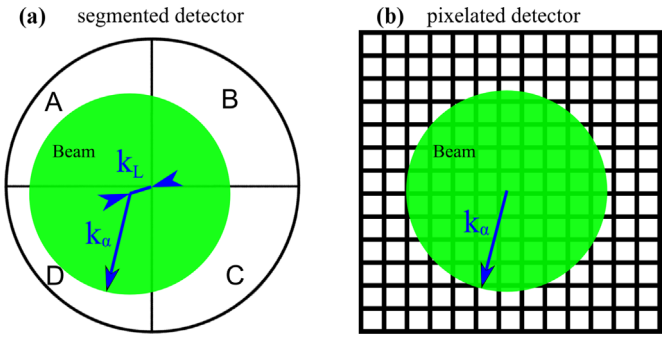

Fig. 4. (a) Schematic of standard 4 quadrant DPC detector and (b) a pixelated detector. The probe radius k_α is indicated along with the deflection k_L arising relative to the centre of the quadrant detector.

by taking difference signals from opposite segments i.e. (A + B) − (C + D) and (A + D) − (B + C). Bright field images were obtained by adding all 4 segments (A + B + C + D). Images of these combinations are displayed in real-time with the Gatan system as the images are acquired. In order to allow comparison to be made, the same probe convergence semi-angle and camera length were used for experiments involving the CCD camera. The projected disc had ~600 pixels diameter after binning. In the pixelated datasets a scanning pixel spacing of 5 nm was used, compared to 2.5 nm pixel steps in standard DPC. The pixelated scan was undersampled due to the practical limit of 100×100 diffraction disk acquisition and need to image field of view big enough for comparison with standard DPC.

For comparison the geometry of the pixelated detector is shown schematically in Fig. 4(b). Rather than recording and combining signals an image of the disk is obtained at each point in the scan. The image set can then be interrogated to extract information regarding the position of the disk. Such an arrangement where a pixelated detector has been used to reproduce the segmented DPC detector geometry has been proposed previously to map stray fields and domains in a single crystal material [18]. In the present work however we will explore techniques which allow intensity variations present in the disk, due to the differential scattering from the small polycrystallites, to be taken out of the image formation by analysis of the data by mathematical algorithms.

Fig. 5 shows images obtained from a domain wall by standard DPC imaging on the permalloy doped film. In (a) the summed quadrant signal, effectively a bright field image can be seen showing the granular structure of the film. While in (b) a difference quadrant image shows the induction component parallel to the length of the wall. Again one can see the large non-magnetic

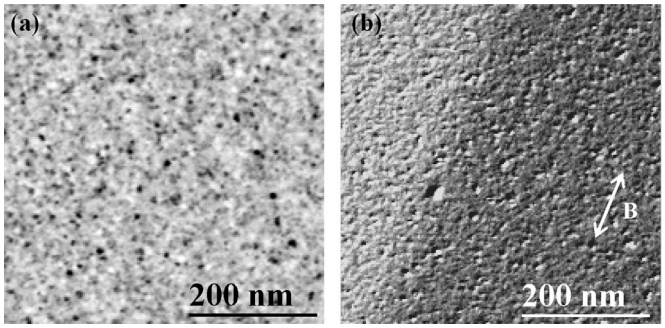

Fig. 5. DPC images acquired from a domain wall in a 20 nm thick permalloy film doped with 5% platinum, (a) bright field image (sum of quadrant signals) and (b) difference signal showing integrated magnetic induction component as indicated by double headed arrow.

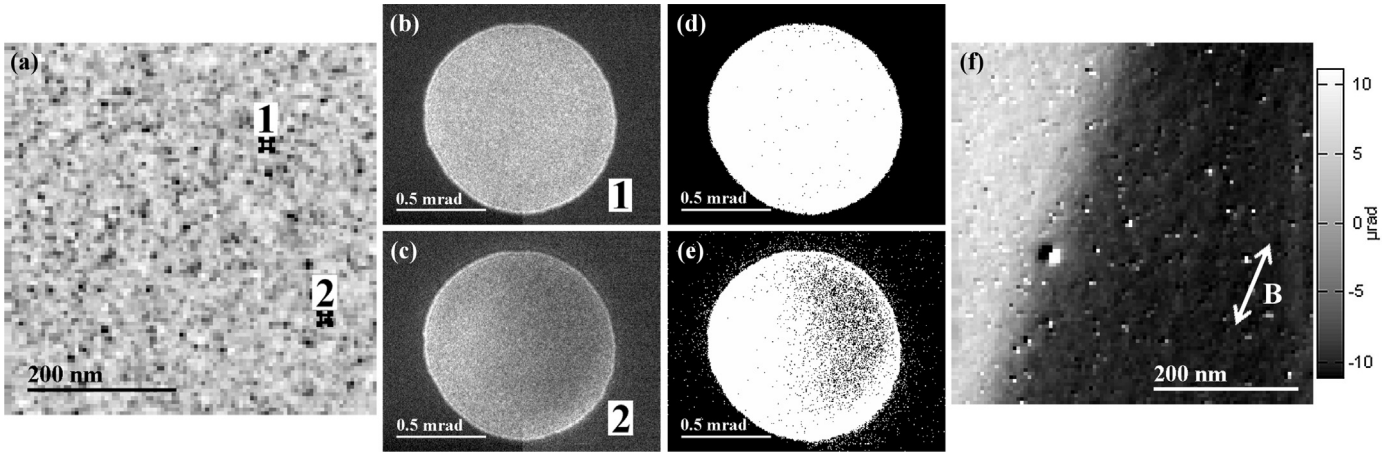

Fig. 6. Centre of mass analysis; (a) bright field image generated by sum of 100×100 diffraction disk images, (b) and (c) example of disk images from pixels highlighted in bright field image labelled 1 and 2, (d) and (e) result of threshold algorithm of the same images, and (f) resulting image of component of integrated magnetic induction along domain wall after processing with centre of mass algorithm.

contributions in this image. DPC imaging with a segmented detector can be considered as measuring the position of the disk on the detector. If the BF disk is assumed to be of uniform intensity the DPC images could be considered as a measure of the centre of mass of the disk. Of course with the diffraction contrast giving the large intensity variations within the disk this assumption breaks down and we therefore see the magnetic information but with added unhelpful crystalline contrast. As an interesting aside, for imaging on a different lengthscale, we note that for atomic scale DPC imaging the centre of mass method has been proven effective when a non-uniform BF disk results from the atomic electric fields [19] where no disk deflection was observed. As will be demonstrated in the following sections, the pixelated detector allows substantial separation of phase and structural (diffraction related) information.

4.1. Centre of mass disk deflection registration

Probably the simplest approach to extract the position of the centre of the circular diffraction disk is to threshold the signal. This should create a binary mask for which the centre of intensity algorithm will be applied:

$$\mathbf{X} = \frac{\sum_i \mathbf{x_i}\,\mathbf{I_i}}{\sum_i \mathbf{I_i}}$$

where $\mathbf{x_i}$ is the position of the pixel and I_i is its corresponding intensity. The result $\mathbf{X} = (x, y)$ gives the position of the centre of the disk. This is done for all 100×100 images of the central diffraction disk. In principle this should result in a set of uniform intensity white disk images, which can then be easily analysed to obtain the 2 orthogonal displacement components. The displacement can be expressed as an absolute value of deflection angle, β_L, as the disk diameter is given by 2α which acts as a calibration. The deflection can then be converted to an integrated induction through Eqs. (1) and (2). An illustration of the methods used here is applied to a region of the sample containing a 180° domain wall. In Fig. 6(a) the bright field image is shown which has been calculated from the 100×100 image set using the acquired data. To further illustrate the data we label 2 points on this image from which we display the diffraction images and these are shown in Figs. 6(b) and (c), these represent a disk with (a) almost constant intensity and (b) one with a typically large intensity variation. We note that the intensity variation within the disk was not connected to the domain wall, where no systematic intensity variation was observed within the disk. For these images a threshold is applied in an attempt to create top hat patterns for the disks. The results for these are shown in Figs. 6(d) and (e) respectively. However due to the signal variation and noise present neither disk data produces a completely perfect top hat function, though clearly Fig. 6 (d) is a better representation than Fig. 6(e). Applying this threshold to the whole data set, the position of the centre of intensity can then be calculated for each point. The displacement can be mapped as two orthogonal directions and so two integrated induction components. The orientation of the two directions was adjusted to map the components along and perpendicular to the domain wall. The resulting integrated induction component mapping the component parallel to the domain wall is shown in Fig. 6(f). While it is apparent that the threshold algorithm does not work perfectly to produce uniform disk images for analysis, the improvement over the DPC image is powerfully evident when comparing Fig. 5(b) and Fig. 6(f). As a first approach this has had significant success in enhancing diffraction contrast filtering compared to standard DPC. We now explore another possible method to further improve the diffraction contrast suppression.

4.2. Cross-correlation disk deflection registration

While the threshold and centre of mass method in the previous section showed an improvement of the magnetic contrast further processing of the data was explored to overcome some of the problems encountered with the variation in intensity observed in the disk. As suggested by [20], edge filtering and cross-correlation can be advantageous and simple to use in electron microscopy. In that investigation the problem of automating image registration due to spatial drift during long period image acquisition, for energy filtered imaging, was tackled successfully using a smoothing kernel and Sobel operator. This made cross-correlations easier for image registration. In our work a simple application of this technique to the diffraction disk position movement allows accurate location of the disk edges for each diffraction image. The smoothing kernel and Sobel operator of 3×3 size were applied to acquired diffraction disks. Here we are imaging effectively the same pattern in each image, hence this filters shot noise and any small variations of the edge of central diffraction disk. Application of these operations to the two disk images in Fig. 6 is reproduced in Fig. 7(a) and (b) resulting in edge images, Figs. 7(c) and (d) respectively. While the original intensity variations in the disks show some resulting intensity variation around the edge images, the locations of the disks are accurately identified. Resulting edge

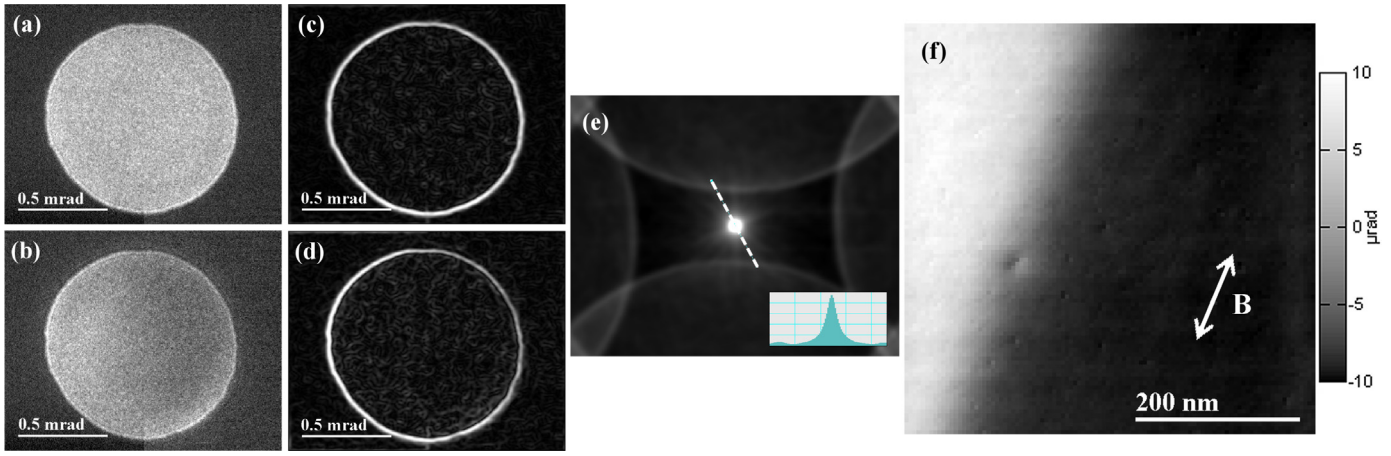

Fig. 7. Cross-correlation image registration; (a) and (b) images of same disk as in previous analysis, (c) and (d) edge pattern generated by smoothing and Sobel algorithm, (e) cross-correlation pattern of edge (d) with ideal disk edge, with line profile detail (f) resulting map of integrated magnetic induction generated from positions of maxima of cross-correlation patterns.

patterns were cross-correlated with the image of ideal disk edge. This was generated by thresholding of one disk from the dataset, smoothed to fit beam edge dispersion and as final step the Sobel algorithm was used to generate ideal edge profile. The position of the maxima of the cross-correlation pattern then corresponds to the disk deflection. An example of a cross-correlation pattern is shown in Fig. 7(e). Displacement measurements extracted from the edge images then reveal an induction variation at the domain wall as shown in Fig. 7(f). The improvement over the thresholding and centre of mass algorithm is powerfully evident. We compare the images quantitatively in the next section.

One of the main difficulties of this approach is that the calculation of the displacement, and hence the deflection, is that it is rounded to integer pixel values. This is unsatisfactory for precise measurements as the maximum displacement for the example given here was 5 pixels. However this analysis can be enhanced by interpolating and curve fitting of the cross-correlation pattern suggested by other studies involving image alignment [21–23]. A script developed with Gatan imaging software [22] was used for interpolation. In simple terms the script works by reading neighbouring pixels of the maxima of the cross-correlation pattern, which are used to interpolate the position of maxima of a second order parabola for both orthogonal deflections. In our case this compares similar edge structures and so any non-linearity associated with this approach can be ignored.

Another option applied to electron microscopy images suggested by [20] is to up-scale the pixelation of the diffraction images and then apply the cross-correlation. In this situation this is impractical due to the constraints of memory and data handling. If scaled to achieve decimal registration, this operation will involve ~1000 GB of data to be processed, with further complications coming from scaling complexity of cross-correlation. To check the quality of image registration we looked at the standard deviation from a uniformly magnetised region such as the bottom right area in Fig. 7(f). The calculated standard deviation for this uniform area was 4% of detected deflection signal, which corresponds to only 0.09 pixel. Such a variation can be attributed to, for example the stability of long scanning acquisition and any small uncorrected descan effects.

A further point to note is that the smoothing of the 3×3 kernel size can impose nonlinearities in registered position. For this dataset the deflection of the beam was in the range of a few pixels, so this was not a problem here. However if the deflection of the disk is rather small and subpixel accuracy becomes essential (imaging of materials with small in-plane magnetic induction), the 3×3 kernel may not be satisfactory for smoothing. This imposes limits on the sensitivity of the system. We show how this can be improved for subpixel accuracy at the end of the next section when we present initial results from the Medipix3 detector, where a higher resolution probe is used. In such a case when the maximum disk displacement becomes close to the pixel size it is necessary to replace the 3×3 kernels with functions which provide greater precision.

5. Discussion

We now compare the results from the images quantitatively to demonstrate and justify the approaches we have proposed for the improvements to the images. Fig. 8 shows a comparison of the images and intensity line profiles obtained by standard DPC, together with the thresholding centre of mass and edge filtering algorithms. Firstly Fig. 8(a) is a standard DPC image together with a single linetrace across the domain wall as shown in Fig. 8(b). The intensity has been calibrated to electron deflection angle as indicated to the right hand side of the images. It is evident that while the domains are visible by eye in the image, the small scale signal variation due to the crystallites masks the wall profile in the linetrace. From the same image but averaging over 80 lines (200 nm in length) as shown in Fig. 8(c) we can see a better representation of the magnetic signal variation across the domain wall, visible in Fig. 8(d). This is possible for a 1D object such as a straight domain wall, but a considerable signal variation from the crystallites is still present. Moving on to the thresholding and centre of mass algorithm image and single linetrace in Figs. 8(e and f), we can see the magnetic signal variation much more easily. Further improvement in the visibility of the magnetic signal variation using the edge detection and cross-correlation is seen in Figs. 8(g and h) where the difference compared to the standard DPC image is clearly evident. Results of least square fitting of the 180° domain wall profile for the 3 methods are compared in Table 1 where the wall induction profiles are fitted to a 1D hyperbolic tangent function, with a width fitting parameter A, i.e. $B = B_s \tanh(x/A)$ [24]. The results are consistent with each other although the increased precision of the measurements, particularly for the edge filtering method is clear. For reference a 20 nm thick permalloy film should have a maximum deflection of 12.7 μrad, given the variation in thickness and moment associated with sputtered materials the measured values are consistent with these parameters.

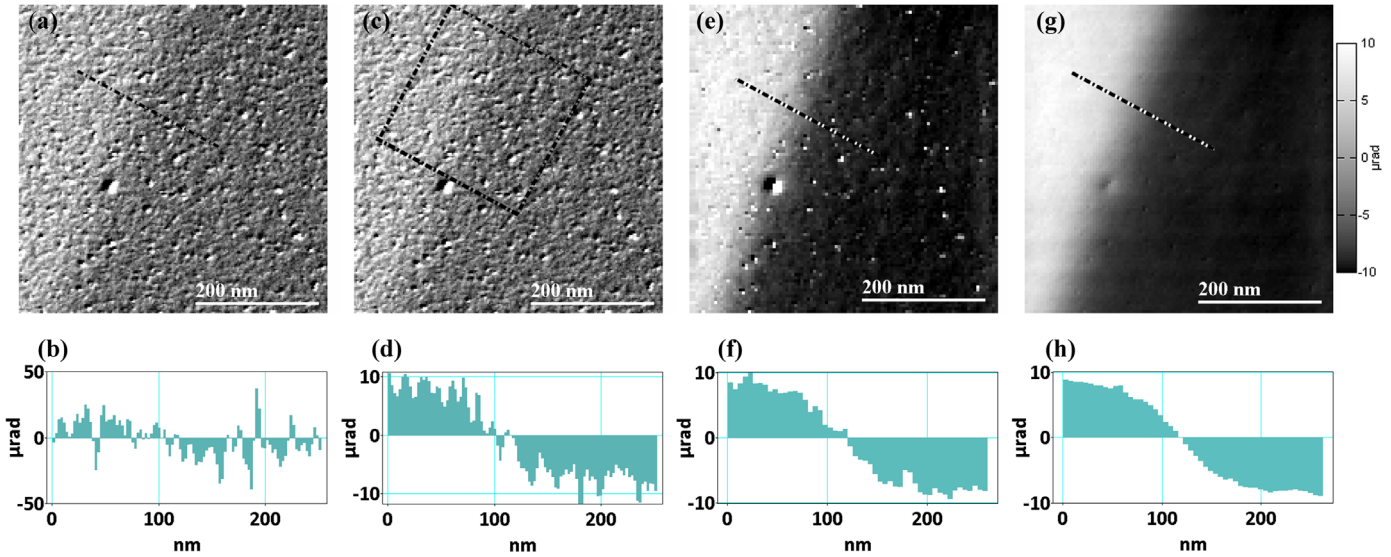

Fig. 8. Comparison of digitally corrected magnetic induction of 180° domain wall. (a) and (b) standard DPC image and its profile, (c) and (d) same image with 80 line average profile, (e) and (f) centre of mass result with its profile, (g) and (h) cross-correlation result with its profile. Quantification of the grey scale of the images is shown in the right of image (g).

Table 1
Comparison of measured domain wall width fitting parameter A (from 1D hyperbolic tangent function) using least squares. The measurements were made from the profiles in Fig. 8(d) (DPC), Fig. 8(f) (centre of mass method) and Fig. 8(h) (edge filtering method).

Method	A [nm]
DPC	44 ± 5
Centre of mass	46 ± 4
Cross-correlation	48 ± 1

The goal of the methodology employed here has been an attempt to remove the intensity variations due to the high spatial frequency effects of the scattering from the crystallites particularly at the boundaries. In doing this we obviously wish to preserve the integrity of the low spatial frequency signal due to the magnetic induction. The magnitude of the crystallite effect on the bright field disk intensity variation is abundantly clear from Figs. 5 and 6. Such is the magnitude of the signal variation that even thresholding to find the disk position by the centre of mass works only up to a point. We have shown a significant improvement on this by using the edge filtering algorithm which demonstrates a step change in what can be achieved for thin magnetic polycrystalline films. While further work and analysis is required it would appear that this type of processing of the diffraction data represent a super efficient version of the modified DPC imaging set up. It was previously found [8] that the best imaging with an annular detector for low spatial frequency magnetic signals occurred when the ratio of radii of the inner hole of the annulus to that of the bright field disk (k_i/k_α) was close to unity. In effect the edge filtering and cross-correlation appear to represent a modified DPC set up with a value of virtually unity in so much as it allows the determination of the disk position very accurately by removing the diffraction effects. We aim to further quantify this effect in future work.

In Fig. 9 we show an example of pixelated DPC imaging from reconstructing disc images acquired using the Medipix3 detector. STEM imaging was performed with a probe convergence semi-angle of $\alpha = 2.2$ mrad corresponding to a spatial frequency of $(0.8\ \text{nm})^{-1}$. The STEM image pixel spacing was 4.9 nm representing

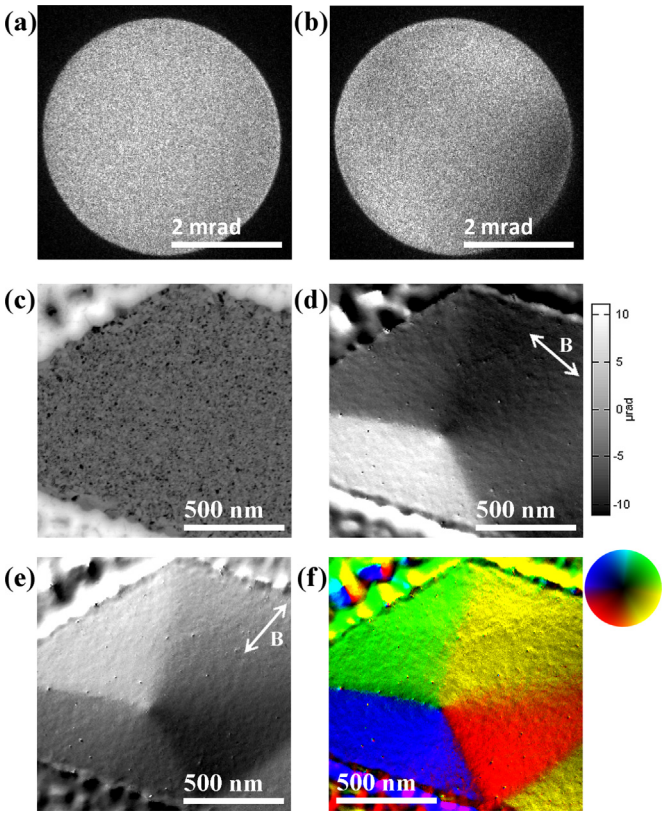

Fig. 9. Example of subpixel resolution with images acquired with the Medipix3 detector. (a) and (b) are examples of BF disk images showing typical intensity variations observed for acquisition times of 1 ms (c) bright field reconstructed image, (d) and (e) are DPC images mapping induction components indicated by the double headed arrows, (f) RGB colour image with wheel showing integrated in-plane magnetic field direction and magnitude. (For interpretation of the references to color in this figure caption, the reader is referred to the web version of this paper.)

an undersampled imaging condition. Data acquisition took ~2 min for 256 × 256 resulting image files. The Medipix3 detector was operated in single pixel mode with a 1 ms acquisition time and

0.85 ms read out time. This gives a speed improvement ratio of ~35 over CCD camera acquisition and we expect to improve this further by investigating where rate limitations are occurring for data transfer. Fig. 9 is produced through analysis of an ~8 GB raw uncompressed dataset, which took 7 min to analyse using a compiled and improved version of the algorithm presented. To illustrate the improvement over the CCD disk detection we show, in Figs. 9(a) and (b) the detected disk with intensity variation similar to those shown in Fig. 6 for the CCD. It should be noted that the individual images here were acquired in 1 ms compared to 50 ms for the CCD in Fig. 6. Fig. 9(c) shows the bright field STEM image produced by summing the pixel intensities for each disc image. To produce Figs. 9(d–f) the disc shift registration method was the same as presented already in previous section for the edge detection. However the accuracy of the edge detection method with the previously used Sobel filter (3×3 kernel) gave imprecise results for the pixel displacements here, which were less than one pixel. Using a suggestion from previous work to improve spatial drift correction [20] we replaced the Sobel filter, employed in Fig. 7, by a convolution with the gradients of a 2D Gaussian function of the same size as the source image. The edge image is provided from the magnitude of resulting images, which then allows displacement measurement by the cross-correlation method to a far greater precision than the Sobel filter, indeed subpixel precision is possible with this procedure. The total deflection of the electron disc in Fig. 9 was 1.1 pixels across all orientations of the magnetic domains present. Thus, by improving our approach, we have shown that accurate subpixel detection of disc shifts is possible.

6. Conclusions

Problems with diffraction contrast from polycrystalline films have long been a problem for STEM DPC imaging of magnetic thin films. Hardware improvements such as an annular quadrant detector help to an extent, however we have shown in this paper that the combination of a pixelated detector and software processing of the bright field disk images gives a huge improvement in the efficiency with which the magnetic phase information can be imaged. This can be achieved even with a standard CCD camera and demonstrated impressively when the edge detection is used, however the acquisition rates are prohibitive for this arrangement. The way forward with this technique is to use a direct radiation detector which brings down the acquisition time by more than an order of magnitude. While earlier work showing superior performance for an earlier Medipix2 detector over CCD detection has been demonstrated [25] we have now applied the functionality to differential contrast phase imaging where the small disk displacements are the key measurement. The sensitivity to the very small Lorentz deflections has been clearly shown, this is a very important improvement given that many modern magnetic materials are extremely thin and often are magnetised perpendicular to the plane of the film. Sub-pixel resolution in the detection of the disk movement is crucial and indicates that when imaging magnetic nanostructures the resolution in *k*-space is as important as the real space resolution possible with aberration corrected systems. We are working on improvements in data acquisition and read out together with processing to maximise the speed with which information may be extracted. Furthermore we note that fuller analysis of the bright field disk intensity distribution where there are small scale phase gradient changes requires a more detailed approach. The transfer of information based on periodic phase or simple beam deflections is limited in that sense and warrants further investigation for information transfer at the highest spatial frequencies.

Acknowledgements

We would like to thank University of Glasgow for funding the doctoral training studentship of Matus Krajnak. The experimental work was supported by Engineering and Physical Sciences Research Council, EPRSC Grant nos. EP/I013520 and EP/I011668/1. Additionally we also acknowledge Seagate for financial support which has allowed us to progress this imaging development project. Also we would like to acknowledge Ales Hrabec from University of Leeds for TEM samples used in this investigation. We would like to thank B. Schaffer of Gatan Inc. for useful discussion and help with data analysis. We also thank Quantum Detectors Ltd for technical help with optimisation of the MERLIN readout system. The data presented here is available at http://dx.doi.org/10.5525/gla.researchdata.296.

References

[1] N. Shibata, S.D. Findlay, Y. Kohno, H. Sawada, Y. Kondo, Y. Ikuhara, Differential phase-contrast microscopy at atomic resolution, Nat. Phys. 8 (August) (2012) 611–615.
[2] S. McVitie, J.N. Chapman, Reversal mechanisms in lithographically defined magnetic thin film elements imaged by scanning transmission electron microscopy, Microsc. Microanal. 3 (02) (1997) 146–153.
[3] Y. Aharonov, D. Bohm, Significance of electromagnetic potentials in the quantum theory, Phys. Rev. 115 (August) (1959) 485–491.
[4] N. Dekkers, H.De. Lang, Differential phase contrast in a STEM, Optik 41 (4) (1974) 452–456.
[5] H. Rose, Nonstandard imaging methods in electron microscopy, Ultramicroscopy 2 (1977) 251–267.
[6] J.N. Chapman, The investigation of magnetic domain structures in thin foils by electron microscopy, J. Phys. D: Appl. Phys. 17 (4) (1984) 623.
[7] J. Chapman, P. Batson, E. Waddell, R. Ferrier, The direct determination of magnetic domain wall profiles by differential phase contrast electron microscopy, Ultramicroscopy 3 (0) (1978) 203–214.
[8] J. Chapman, I. McFadyen, S. McVitie, Modified differential phase contrast Lorentz microscopy for improved imaging of magnetic structures, IEEE Trans. Magn. 26 (September) (1990) 1506–1511.
[9] T.J. Pennycook, A.R. Lupini, H. Yang, M.F. Murfitt, L. Jones, P.D. Nellist, Efficient phase contrast imaging in STEM using a pixelated detector. Part 1: experimental demonstration at atomic resolution, Ultramicroscopy (2014).
[10] S. Majert, H. Kohl, High-resolution STEM imaging with a quadrant detector—conditions for differential phase contrast microscopy in the weak phase object approximation, Ultramicroscopy 148 (2015) 81–86.
[11] H. Yang, T.J. Pennycook, P.D. Nellist, Efficient phase contrast imaging in stem using a pixelated detector. Part ii: optimisation of imaging conditions, Ultramicroscopy 151 (2015) 232–239.
[12] M. Haider, H. Rose, S. Uhlemann, B. Kabius, K. Urban, Towards 0.1 nm resolution with the first spherically corrected transmission electron microscope, J. Electron Microsc. 47 (5) (1998) 395–405.
[13] O. Krivanek, G. Corbin, N. Dellby, B. Elston, R. Keyse, M. Murfitt, C. Own, Z. Szilagyi, J. Woodruff, An electron microscope for the aberration-corrected era, Ultramicroscopy 108 (3) (2008) 179–195.
[14] B. Freitag, M. Bischoff, H. Mueller, P. Hartel, H. von Harrach, Sub-nanometer resolution in field-free imaging using a Titan 80-300 with Lorentz lens and iImage Cs-corrector at 300 kV acceleration voltage, Microsc. Microanal. 15 (S2) (2009) 184–185.
[15] S. McVitie, D. McGrouther, S. McFadzean, D. MacLaren, K. O'Shea, M. Benitez, Aberration corrected Lorentz scanning transmission electron microscopy, Ultramicroscopy 152 (2015) 57–62.
[16] R. Ballabriga, M. Campbell, E. Heijne, X. Llopart, L. Tlustos, W. Wong, Medipix3: a 64 k pixel detector readout chip working in single photon counting mode with improved spectrometric performance, Nucl. Instrum. Methods Phys. Res. Sect. A: Accel. Spectrom. Detect. Assoc. Equip. 633 (2011) S15–S18.
[17] R. Plackett, I. Horswell, E. Gimenez, J. Marchal, D. Omar, N. Tartoni, Merlin: a fast versatile readout system for Medipix3, J. Instrum. 8 (01) (2013) C01038.
[18] A. Yasuhara, W. Inami, K. Yamazaki, A. Saitow, K. Okamoto, H. Endo, M. Kawazu, T. Suzuki, I. Ohnishi, Y. Kondo, Observation of magnetic and electric field in STEM by using CCD camera, Microsc. Microanal. 15 (S2) (2009) 1058–1059.
[19] K. Müller, F.F. Krause, A. Béché, M. Schowalter, V. Galioit, S. Löffler, J. Verbeeck, J. Zweck, P. Schattschneider, A. Rosenauer, Atomic electric fields revealed by a quantum mechanical approach to electron picodiffraction, Nat. Commun. 5 (2014).
[20] B. Schaffer, W. Grogger, G. Kothleitner, Automated spatial drift correction for {EFTEM} image series, Ultramicroscopy 102 (1) (2004) 27–36.
[21] M. Guizar-Sicairos, S.T. Thurman, J.R. Fienup, Efficient subpixel image registration algorithms, Opt. Lett. 33 (2) (2008) 156–158.

[22] V. Hou, Cross Correlate Plugin, ⟨http://donation.tugraz.at/dm/source_codes/144⟩, 2008.
[23] P. Bing, X. Hui-Min, X. Bo-Qin, D. Fu-Long, Performance of sub-pixel registration algorithms in digital image correlation, Meas. Sci. Technol. 17 (6) (2006) 1615.
[24] S. McVitie, J. Chapman, Measurement of domain wall widths in permalloy using differential phase contrast imaging in stem, J. Magn. Magn. Mater. 83 (1) (1990) 97–98.
[25] G. McMullan, D. Cattermole, S. Chen, R. Henderson, X. Llopart, C. Summerfield, L. Tlustos, A. Faruqi, Electron imaging with Medipix2 hybrid pixel detector, Ultramicroscopy 107 (4–5) (2007) 401–413.